Light scattering by a multicomponent plasma coupled with longitudinal-optical phonons: Raman spectra of *p*-type GaAs:Zn

G. Irmer, M. Wenzel, and J. Monecke
Institute of Theoretical Physics, University of Mining and Technology, D-09596 Freiberg, Germany
(Received 2 August 1996; revised manuscript received 27 January 1997)

The LO-phonon–hole-plasmon coupling is investigated for *p*-type III-V semiconductors. Due to a large carrier damping, only one coupled LO-phonon–plasmon mode (CPPM) appears. Expressions for the theoretical Raman scattering efficiency of a multicomponent plasma are derived in the random phase approximation. They take into account wave-vector-dependent intraband transitions within the heavy- and light-hole bands as well as interband transitions between them. Finite lifetime effects were included in a generalized Mermin approximation. The theoretical band shapes of the CPPM at different temperatures are compared with Raman measurements of Zn-doped *p*-type GaAs in the hole concentration range $p=10^{17}$–10^{20} cm^{-3}. At low temperatures the contribution of the interband transitions cannot be neglected in the frequency range of the CPPM, resulting in a mode broadening. Agreement between the theoretical band shapes and the Raman spectra is obtained without any fit parameter if the hole concentration p and the mobility μ are derived from the measured Hall values p_H and μ_H evaluated on the basis of a two-band model of the conductivity. Raman measurements of the CPPM in Zn-doped *p*-type GaP show a different temperature dependence, which is explained by the different ratio of the light- to the heavy-hole effective mass on the interband transitions. [S0163-1829(97)01536-1]

I. INTRODUCTION

In polar semiconductors the plasmons of free carriers interact with the longitudinal-optical (LO) phonons via their macroscopic electric fields. The resulting coupled LO-phonon–plasmon modes (CPPM's) were first discussed by Varga[1] and observed in the Raman spectra of *n*-type GaAs by Mooradian and Wright.[2] Since then the CPPM's have been intensively studied from both theoretical and experimental viewpoints. Methods of the electrical characterization of polar semiconductors based on the analysis of the CPPM measured by Raman scattering or far-infrared spectroscopy have been established. By far most work has dealt with *n*-type III-V semiconductors of high carrier mobilities and low carrier effective masses, where a low-energy branch (L_-) and a high-energy branch (L_+) of the CPPM can be observed. Relatively little work has been reported on the CPPM in *n*-type polar semiconductors with low carrier mobilities and higher effective electron masses.[3–7] In this case only one overdamped CPPM appears, for which frequency shift and halfwidth broadening are small in comparison with the values of the pure LO phonon. Hence, the finite lifetime of the lattice vibrations has to be included in the analysis of the CPPM.

In *p*-type polar semiconductors, the situation is much more complicated. Besides a lower carrier mobility than in most *n*-type semiconductors, different sorts of free holes contribute to the free-carrier plasma. For example, in *p*-GaAs only about 5% of the free carriers are present as light holes. However, because their plasmon energy is about 38% of that of the heavy-hole plasmon energy and because of their higher mobility, the influence of the light holes on the optical and electrical properties of the plasma is important. A theoretical treatment of the CPPM has to take into account LO phonons, light holes, heavy holes, and all their interactions.

In an earlier work Olego and Cardona[8] investigated the Raman scattering by coupled LO-phonon–plasmon modes in heavily doped *p*-type GaAs:Zn with hole concentrations ranging from 10^{17} to 10^{20} cm^{-3}. They interpreted their results by wave-vector nonconservation and a breakdown of the selection rules due to scattering by ionized impurities. Kamijoh *et al.*[9] investigated *p*-type GaAs:Si with carrier concentrations of 6×10^{16}–3×10^{18} cm^{-3}. They proposed that long-wavelength CPPM could not be observed due to the low mobility of about 20 cm^2/V s. The phonon mode observed at the unchanged LO-phonon frequency was interpreted as the $L_-(q)$ mode at large wave vector[9] due to scattering by heavily doped ionized impurities. Its broadening was explained by the impurity-induced Fröhlich interaction, similar to Ref. 8.

Yuasa and Ishii[10] studied the Raman scattering from Be-doped *p*-type GaAs. They observed for $p=3\times10^{18}$ cm^{-3} a shoulder on the high-frequency side of the LO-phonon mode and for $p=2\times10^{19}$ cm^{-3} a broad peak near the TO phonon (''mode *B*''). By comparison with measurements of the TO-phonon mode from the (110) cleaved surface they concluded that the selection rules are maintained in their molecular-beam epitaxy (MBE)-grown layers and that the mode *B* should not be identified with the forbidden TO phonon but with the low-frequency branch of the CPPM.

Mlayah *et al.*[11] performed Raman measurements on GaAs:Be samples with very high doping levels ranging from 10^{19}–1.4×10^{21} cm^{-3}. They observed a single CPPM in the vicinity of the TO-phonon frequency. By means of a line-shape analysis, which took into account plasmon damping, the carrier densities of the samples were determined.

 © 1997 The American Physical Society

Wan and Young[12] investigated Be-doped samples in the carrier concentration range from 1.1×10^{18}–3×10^{19} cm^{-3} and stated a single-mode behavior primarily due to the overdamped nature of heavy-hole intraband transitions. They compared their Raman scattering spectra with a theory similar to that derived by Hon and Faust[3] and Klein *et al.*[13] for the one-carrier sort only. Intraband contributions were included in the Lindhard-Mermin[19] form for a Maxwell-Boltzmann distribution of the free carriers, and interband transitions were taken into account using an expression of Bardyszewski[14] in the limit of zero wave vector generalized to finite temperature. The carrier concentrations obtained from the fits of the Raman spectra were compared with Hall measurement data.

More recently Fukasawa and Perkowitz[15] have reported Raman spectra of Be-doped MBE-grown p-type GaAs with hole concentrations between 6.3×10^{17} and 1.9×10^{19} cm^{-3}. They analyzed the band shapes by comparison with theoretical expressions.[2,15] From the band fits hole mobilities μ_R were obtained using fixed p values from Hall measurements. The ratio between the Hall mobilities μ_H and the mobilities from the Raman measurements was found to be $\mu_H/\mu_R=1.5-2.6$ depending on the hole concentration. A similar enhancement of the hole mobilities obtained by Raman measurements in comparison with Hall mobilities was reported by Gargouri *et al.*[16] ($\mu_H/\mu_R=3.7$), Mlayah *et al.*[11] ($\mu_H/\mu_R\approx2$), and Irmer *et al.*[17] ($\mu_H/\mu_R\approx2.3$).

In this work the differences between the results of electrical and optical measurements in p-type semiconductors are discussed on the basis of a two-band model of the free holes.

In Sec. II the system of coupled polarizations of electrons and LO phonons, considered, e.g., by Klein *et al.*,[18,13] is generalized to a multicomponent plasma. The Raman cross section is derived in random-phase approximation (RPA). It takes into account the wave-vector dependence of the scattering as well as finite lifetime effects in the relaxation-time approximation. The interpretation of Raman measurements in p-type semiconductors at low temperatures requires a dielectric function that includes intraband as well as interband transitions (Sec. III). A generalization of the Mermin procedure[19] was used.[20] In Sec. IV the connections between the Hall and the drift values of the free hole concentration and mobility are discussed. The Raman measurements were performed on Zn-doped GaAs with dominating impurity scattering of the holes in the concentration range $p=10^{18}$ – 10^{20} cm^{-3} at different temperatures. In Sec. VI the results of the Raman measurements are compared with the theoretical Raman cross sections. It is shown that the theoretical cross sections describe the experimental results well. At low temperatures the interband transitions are proven to make important contributions.

II. RAMAN-SCATTERING EFFICIENCY

The cross section of light scattering can be written in terms of the matrix elements of the transition susceptibility operator and is given by[21–23,53]

$$I=\frac{\partial^2\sigma}{\partial\Omega\,\partial\omega}=\left(\frac{\omega_s}{c}\right)^4\left(\frac{\omega_s}{\omega_l}\right)^2\frac{V^2}{2\pi}\int dt\,e^{i\omega t}\langle i|\,\delta\chi(\mathbf{q},t)\,\delta\chi^{\dagger}(\mathbf{q},0)|i\rangle_T. \tag{1}$$

$\omega=\omega_l-\omega_s$ is the scattering frequency, ω_l the frequency of the incident laser light, ω_s the frequency of the scattered light, V the scattering volume, and Ω the room angle. The scattering wave vector $\mathbf{q}$ is given by $\mathbf{q}=\mathbf{q}_l-\mathbf{q}_s$. $\delta\chi$ is the transition susceptibility operator of the crystal in the Heisenberg representation given below. $\langle\ \rangle_T$ denotes the thermal ensemble average over the initial states.

In the transition susceptibility, contributions of the free carriers and of the phonons are involved.

For the calculation of the transition susceptibility at $q\simeq0$, two mechanisms of the electron-lattice interaction have to be considered. The deformation-potential interaction, leading to the contribution $\delta\chi_u$, is due to the modulation of the periodic crystal potential by the relative displacement of the atoms in the unit cells. The Fröhlich interaction of the carriers with the longitudinal macroscopic electric field $\mathbf{E}^L$ associated with the longitudinal-optical polar phonons causes another contribution $\delta\chi_E^L$ to the transition susceptibility:

$$\delta\chi_u=\left(\frac{\partial\chi}{\partial u}\right)u(\mathbf{q})=\sum_{i,j,k}e_i^l e_j^s e_k^q\left(\frac{\partial\chi_{ij}}{\partial u_k}\right)u(\mathbf{q}), \tag{2}$$

$$\delta\chi_E^L=\left(\frac{\partial\chi}{\partial E^L}\right)E^L(\mathbf{q})=\sum_{i,j,k}e_i^l e_j^s e_k^q\left(\frac{\partial\chi_{ij}}{\partial E_k^L}\right)E^L(\mathbf{q}). \tag{3}$$

$\mathbf{e}^l(\mathbf{e}^s)$ are the incident and scattered photon polarization unit vectors; $\mathbf{e}^q=\mathbf{q}/|\mathbf{q}|$ is the unit vector parallel to longitudinal displacements. $(\partial\chi_{ij}/\partial u_k)$ and $(\partial\chi_{ij}/\partial E_k^L)$ are the elements of the Raman tensor and the electro-optical Raman tensor, respectively.

In the $q\simeq0$ quasistatic approximation both contributions are assumed to be q independent.

For simplicity we assume that the free carriers of the type i move in a parabolic band with effective mass tensor $\tilde{m}_i^*$. Their contribution to the transition susceptibility in addition to Eqs. (2) and (3) is

$$\delta\chi_{\rho i}=\frac{r_e c^2}{\omega_s^2}\mu_i\rho_i(\mathbf{q}), \tag{4}$$

with

$$\mu_i=\mathbf{e}^l\cdot\left(\frac{m_o}{m_i^*}\right)\cdot\mathbf{e}^s=\sum_{j,k=1}^{3}e_j^l e_k^s\left(\frac{m_o}{m_i^*}\right)_{jk},$$

$$m_i^*=m_o m_i; \tag{5}$$

$r_e=(e^2/4\pi\varepsilon_o m_o c^2)$ is the classical radius of the electron.

$\rho_i(\mathbf{q})=(1/V)\Sigma_j e^{i\mathbf{q}\cdot\mathbf{r}_{ij}}$ is the Fourier transform of the free-carrier density operator. The sum extends over all free carriers of type i.

The Born effective charges e^* associated with the displacements $u(\mathbf{q})$ produce dipole fields with the qth Fourier

component of the polarization given by

$$P_o(\mathbf{q})=\frac{e^*u(\mathbf{q})}{V}. \tag{6}$$

The free-carrier polarization is related to $\rho_i(\mathbf{q})$ by Poisson's equation:

$$P_i(\mathbf{q})=\frac{e_i\rho_i(\mathbf{q})}{iq} \tag{7}$$

with $e_i=+e(-e)$ in the case of free holes (electrons), respectively.

The total polarization $P=P_o+\Sigma_{i=1}^{n_c}P_i$ is screened by the bound electrons and produces the longitudinal macroscopic field E^L with the Fourier component

$$E^L(\mathbf{q})=-\frac{P(\mathbf{q})}{\varepsilon_o\varepsilon_\infty}. \tag{8}$$

Therefore, the total transition susceptibility as a function of the polarizations is obtained as

$$\delta\chi=\frac{V}{e^*}\left(\frac{\partial\chi}{\partial u}\right)P_o-\frac{1}{\varepsilon_o\varepsilon_\infty}\left(\frac{\partial\chi}{\partial E^L}\right)\left(P_o+\sum_{i=1}^{n_c}P_i\right)+\frac{iqr_ec^2}{e\omega_s^2}\sum_{i=1}^{n_c}\mu_iP_i. \tag{9}$$

The calculation of the cross section [Eq. (1)] can be carried out using the fluctuation-dissipation theorem. In the case of the system of coupled longitudinal polarizations we obtain

$$\sum_{i,j}c_{ij}\frac{V^2}{2\pi}\int dt\,e^{i\omega t}\langle i|P_i(\mathbf{q},t)P_j^\dagger(\mathbf{q},0)|i\rangle=\frac{\hbar}{\pi}(n_\omega+1)\sum_{i,j}c_{ij}\mathrm{Im}\{T_{ij}(\mathbf{q},\omega)\} \tag{10}$$

with the linear-response function matrix T_{ij}. $n_\omega+1=[1-\exp(-\hbar\omega/kT)]^{-1}$ is the Bose-Einstein statistical factor. Externally applied fictious driving fields $D_i(\mathbf{q},\omega)$, which act on the ionic and carrier subsystems, are introduced with the aim of evaluating these response functions.

The interaction within and between the subsystems can be taken into account in the random-phase approximation by linear response to the total effective electrical fields

$$E_i(\mathbf{q},\omega)=D_i(\mathbf{q},\omega)-\frac{1}{\varepsilon_o\varepsilon_\infty}\sum_{j=0}^{n_c}P_j(\mathbf{q},\omega), \tag{11}$$

where the Fourier components of the polarizations are given by

$$P_i(\mathbf{q},\omega)=\varepsilon_o\chi_i(\mathbf{q},\omega)E_i(\mathbf{q},\omega). \tag{12}$$

χ_i are the electrical susceptibilities of the subsystems. The solutions of Eqs. (11) and (12) are

$$P_i(\mathbf{q},\omega)=\frac{1}{V\varepsilon_o}\sum_j T_{ij}(\mathbf{q},\omega)D_j(\mathbf{q},\omega) \tag{13}$$

with

$$T_{ij}=V\varepsilon_o(\chi_i\delta_{ij}-\chi_i\chi_j/\varepsilon), \tag{14}$$

where

$$\varepsilon(\mathbf{q},\omega)=\varepsilon_\infty+\sum_{i=0}^{n_c}\chi_i \tag{15}$$

is the total dielectric function for electrical fields. The coefficients c_{ij} in Eq. (10) are evaluated to be given by

$$c_{oi}=c_{io}=b^2a_o^2, \tag{16}$$

$$c_{ij}=a_o^2+a_ia_j;\quad i,j\neq 0 \tag{17}$$

with

$$a_o=-\frac{1}{\varepsilon_o\varepsilon_\infty}\left(\frac{\partial\chi}{\partial E^L}\right),$$

$$b=1-C_{\mathrm{FH}}\frac{\omega_T^2}{\omega_L^2-\omega_T^2}, \tag{18}$$

$$a_i=-\frac{eq\mu_i}{4\pi\varepsilon_om_o\omega_s^2}. \tag{19}$$

In Eq. (18) we introduced the Faust-Henry coefficient, which describes the contribution ratio of the deformation potential and the electro-optic mechanisms.[13] $\omega_L(\omega_T)$ are the frequencies of the longitudinal (transverse) optical phonons, M their reduced mass. From Eqs. (1) and (10) we obtain in the case of isotropic effective masses

$$I=I_A+I_B=\left(\frac{\partial^2\sigma}{\partial\Omega\,\partial\omega}\right)=\left(\frac{\omega_s}{c}\right)^4\left(\frac{\omega_s}{\omega_l}\right)^2\frac{\hbar(n_\omega+1)}{\pi}\mathrm{Im}(S_A+S_B) \tag{20}$$

with

$$S_A=\frac{V}{\varepsilon_0\varepsilon_\infty^2}\left[\sum_{i,j,k=1}e_i^le_j^se_k^q\left(\frac{\partial\chi_{ij}}{\partial E_k^L}\right)\right]^2\times\frac{1}{\varepsilon}\left\{\varepsilon_\infty b^2\chi_0+[\varepsilon_\infty+(1-b)^2\chi_0]\sum_{i=1}^{n_c}\chi_i\right\}, \tag{21}$$

$$S_B=V\varepsilon_0\left(\frac{eq}{4\pi\varepsilon_0m_0\omega_s^2}\right)^2\left[\sum_i e_i^le_i^s\right]^2\frac{1}{\varepsilon}\left\{(\varepsilon_\infty+\chi_0)\sum_{i=1}^{n_c}\frac{\chi_i}{m_i^2}+\frac{1}{2}\sum_{i,j=1}^{n_c}\left(\frac{1}{m_i}-\frac{1}{m_j}\right)^2\chi_i\chi_j\right\}. \tag{22}$$

The scattering efficiency I of the CPPM has a contribution I_A due to the phonon displacement u and electric field $\mathbf{E}^L$ and a contribution I_B due to the charge-density fluctuation. As mentioned above, we used the dipole approximation. Then the polarizations associated with the sublattice displacements $u(\mathbf{q})$ are real and the free-carrier polarizations imaginary and do not interfere; the scattered intensities simply add. However, if the laser energy is close to a band gap, the dipole-

forbidden Fröhlich scattering becomes important and contributes to the scattering amplitude. In this case the scattering amplitudes are complex, and interference and partial cancelation of the different contributions is possible. Such interference effects were observed and discussed in n-GaAs, for example, by Menéndez and Cardona.[47] In our work we used laser excitation out of resonance; the magnitudes of the contributions of S_A and S_B to the scattering efficiency are added depending on sample and polarization orientation.

We note that Eq. (22) includes the special case of light scattering by a two-component plasma (without phonon interaction), considered in Refs. 24 and 25. Before discussing the light scattering by a multicomponent plasma in a polar semiconductor in the general situation, we prove that Eqs. (20)–(22) reduce to the scattering cross-section expressions obtained earlier for special cases.

III. DIELECTRIC FUNCTION

A. One carrier type, phonon damping neglected, q=0

For small **q**, neglected phonon damping and one free-carrier type of effective mass m^* (isotropic mass tensor) with concentration n and mobility μ the dielectric function can be approximated by

$$\varepsilon=\varepsilon_\infty+\chi_0+\chi_1=\varepsilon_\infty\left(1+\frac{\omega_L-\omega_T^2}{\omega_T^2-\omega^2}-\frac{\omega_P^2}{\omega(\omega+i\Gamma)}\right) \quad (23)$$

with the plasma frequency $\omega_P=(e^2n/\varepsilon_0\varepsilon_\infty m^*)^{1/2}$ and the plasmon damping $\Gamma=e/m^*\mu$. The expressions $\mathrm{Im}(S_A)$ and $\mathrm{Im}(S_B)$ in Eq. (20) reduce to

$$\mathrm{Im}(S_A)=\frac{V}{\varepsilon_0}\left[\sum_{i,j,k=1}^{3} e_i^l e_j^s e_k^q\left(\frac{\partial\chi_{ij}}{\partial E_k^L}\right)\right]^2 \times\left[\frac{\omega_T^2(1+C_{\mathrm{FH}})-\omega^2}{\omega_T^2-\omega^2}\right]^2\mathrm{Im}\left(-\frac{1}{\varepsilon}\right) \quad (24)$$

and

$$\mathrm{Im}(S_B)=V\varepsilon_0\ \frac{\varepsilon_\infty^2}{m_1^{*2}}\left(\frac{eq}{4\pi\varepsilon_0 m_0\omega_s^2}\right)^2\left[\sum_{i=1}^{3} e_i^l e_i^s\right]^2 \times\left(\frac{\omega_L^2-\omega^2}{\omega_T^2-\omega^2}\right)^2\mathrm{Im}\left(-\frac{1}{\varepsilon}\right), \quad (25)$$

which are identical to those obtained, e.g., in Ref. 4. Equations (24) and (25) have been successfully applied by many authors to interpret the light scattering by plasmons in n-type III-V semiconductors with high carrier mobility and scattering excitation in the region of transparency of the samples.

B. One carrier type, phonon damping included, q=0

In semiconductors with low carrier mobilities, i.e., large plasmon damping, instead of two coupled LO-phonon–plasmon modes only one overdamped mode near the LO phonon is observed. If we include the phonon damping γ into the phonon contribution to the electrical susceptibility

$$\chi_0=\varepsilon_\infty\frac{\omega_L^2-\omega_T^2}{\omega_T^2-\omega^2-i\omega\gamma}, \quad (26)$$

the light-scattering efficiencies derived from Eqs. (20)–(22) can be expressed in the form of Eqs. (24), (25) with the prefactors of $\mathrm{Im}(-1/\varepsilon)$ changed (see Appendix A). The light-scattering cross section including phonon damping has been successfully used to determine the carrier concentration and mobility in accordance with electrical measurements, e.g., in n-GaP,[4] ZnSe,[5,6] and SiC.[7]

In cases of large effective carrier masses the light-scattering efficiency I_A via deformation potential and electro-optic mechanisms dominates, and the contribution I_B due to charge density fluctuations is negligible.

Essential features of the influence of the free carrier and of the lattice vibration dampings can be studied by a classical treatment of the coupled phonon-plasmon system with Born-Huang-type equations of motion[25,26] assuming only one carrier type. In the presence of damping the solution of the eigenvalue problem requires complex values of ω. The real and the imaginary parts give the frequencies and the damping rates of the coupled modes, respectively. In order to demonstrate the behavior of these solutions depending on the plasma frequency, two cases of low ($\Gamma=10\ \mathrm{cm}^{-1}$) and high free-carrier damping ($\Gamma=500\ \mathrm{cm}^{-1}$) were calculated (see Fig. 1). For the phonon damping the value $\gamma=1\ \mathrm{cm}^{-1}$ and for the effective mass the value $m^*=0.4m_0$ were used.

For low damping rates (case I in Fig. 1) the coupled modes can be classified in an upper branch L_+ and a lower branch L_- as observed, e.g., in n-type GaAs. With increasing carrier concentration (plasma frequency) the upper mode changes in energy from a phononlike to a plasmonlike character and vice versa for the lower-frequency mode, which reaches the TO-phonon energy for large plasmon energies. The mode dampings show similar tendencies (Fig. 1, case Ib) with $-\mathrm{Im}(\omega)=\gamma$ at $\omega_p=0$ and $-\mathrm{Im}(\omega)=\Gamma$ for $\omega_p\gg\omega_L$ for the upper mode and vice versa for the lower mode. For large plasmon dampings (case II in Fig. 1) the separation into ''upper'' (full circles) and ''lower'' (open circles) is physically meaningless. One mode is more phononlike, with energies $\mathrm{Re}(\omega)=\omega_L$ at $\omega_p=0$ and $\mathrm{Re}(\omega)=\omega_T$ at $\omega_p\gg\omega_L$ and with nearly pure phonon damping in both cases, whereas the other mode is an overdamped plasmon mode.

In this context the simplest approach to describing the Raman scattering efficiency in p-type semiconductors is to take into consideration the contributions χ_1 and χ_2 of the heavy and light holes with concentration $p=p_1+p_2$ to the electrical susceptibility, introducing an effective plasmon frequency ω_p^* and effective damping Γ^*, substituting

$$-\frac{\varepsilon_\infty\omega_{p1}^2}{\omega(\omega+i\Gamma_1)}-\frac{\varepsilon_\infty\omega_{p2}^2}{\omega(\omega+i\Gamma_2)}=-\frac{\varepsilon_\infty\omega_p^{*2}}{\omega(\omega+i\Gamma^*)} \quad (27)$$

with $\omega_p^{*2}=e^2p/\varepsilon_0\varepsilon_\infty m_p^*$ and $\Gamma^*=e/m_\Gamma^*\mu$. $p=p_1+p_2$ is the hole concentration; the ''effective'' masses m_p^* and m_Γ^* introduced in ω_P^* and Γ^* have a weak dependence on the dominating hole scattering process.[27]

With the parameters given in Table I and assuming $m_p^*=m_\Gamma^*=0.43m_0$ dependence of the Raman-scattering efficiency on the plasmon damping Γ^* was calculated.

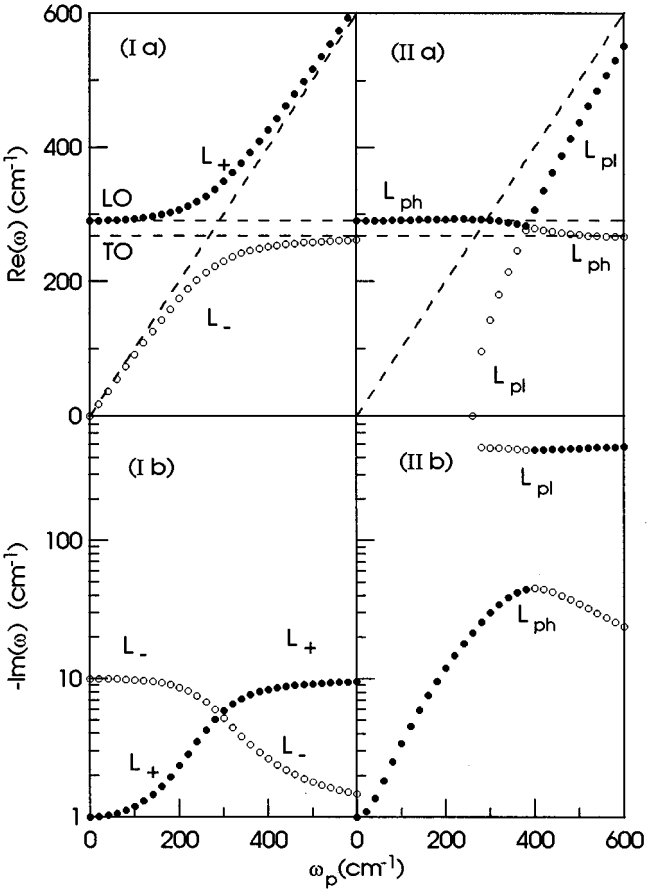

FIG. 1. Real part (a) and imaginary part (b) of the normal mode frequencies of the coupled phonon-plasmon system in dependence on the plasmon frequency assuming one type of carrier. The real part (imaginary part) corresponds to the frequency (damping rate) of the coupled modes. (I) Small plasmon damping (parameters used: $\Gamma=10\ \mathrm{cm}^{-1}, \gamma=1\ \mathrm{cm}^{-1}$). (II) Large plasmon damping (parameters used: $\Gamma=500\ \mathrm{cm}^{-1}, \gamma=1\ \mathrm{cm}^{-1}$). In the calculations $m^*=0.4m_0$ was used.

The maxima of the CPPM obtained are shown in Fig. 2. For dampings $\Gamma^* \gtrsim 100\ \mathrm{cm}^{-1}$ only one coupled mode appears; its maximum shifts to the TO-phonon frequency with increased hole concentration, in qualitative agreement with the experimental results given in Sec. VI. However, the quantitative interpretation of the Raman-scattering spectra obtained at different temperatures, using an excitation wavelength at which the samples are opaque, requires a more refined model of the dielectric function.

C. Two carrier types (holes), interband transitions and dampings included, $\mathbf{q}\neq\mathbf{0}$

In p-type diamond or zinc-blende semiconductors the valence-band top at $\mathbf{k}=0$ is fourfold degenerate and splits for $\mathbf{k}\neq 0$ into the bands of heavy and light holes with masses m_1^* and m_2^*, respectively. Band-structure effects such as nonparabolicities, warping, and the split-off band, separated by spin-orbit coupling, are neglected in the following.

The free holes contribute to the dielectric function by intraband transitions as well as by interband transitions between the two bands. An expression of the ω- and q-dependent RPA dielectric function, which takes into account finite-lifetime effects in a relaxation-time approximation, is given by[28]

$$\varepsilon(\mathbf{q},\omega)=\varepsilon_\infty+\sum_{i=0}^{2}\chi_i=\varepsilon_\infty+\chi_0+\sum_{\nu,\nu'=1}^{2}\chi^{\nu\nu'}, \qquad (28)$$

with the intraband contributions

TABLE I. Parameters used in calculations.

m_1	Heavy-hole effective mass	$0.56m_0$ [a]
m_2	Light-hole effective mass	$0.08m_0$ [a]
ε_∞	High-frequency dielectric constant	10.6 [b]
ε_S	Static dielectric constant	12.8 [b]
ω_T	TO(Γ)-phonon energy	
	at $T=300$ K	268.1 cm^{-1} [c]
	at $T=10$ K	271.8 cm^{-1} [c]
ω_L	LO(Γ)-phonon energy	
	at $T=300$ K	291.4 cm^{-1} [c]
	at $T=10$ K	295.1 cm^{-1} [c]
γ	Phonon damping constant	2 cm^{-1} [c]
C	Faust-Henry coefficient	
	at $T=300$ K	-0.48 [d]
	at $T=10$ K	-0.53 [d]
α	Absorption coefficient	0.80×10^5 cm^{-1} [e]

[a]Reference 44.
[b]Reference 42.
[c]Reference 40.
[d]Reference 43.
[e]Reference 41.

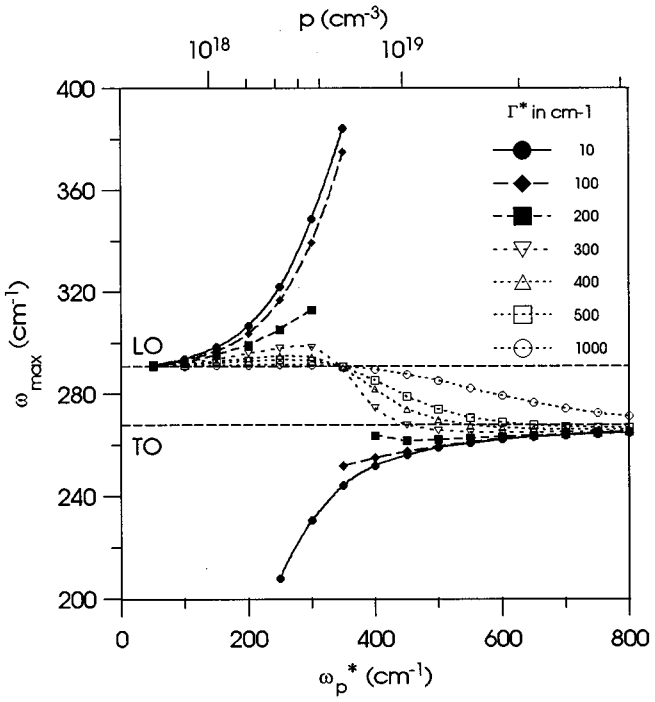

FIG. 2. Maxima of the CPPM according to Eq. (21) depending on the plasma frequency. The parameter in the figure is the plasmon damping. The calculations were performed with $m^*=0.4$, assuming one carrier type.

$$\chi^{\nu\nu}=\frac{\tilde{\chi}^{\nu\nu}(\mathbf{q},\omega+i\Gamma_\nu)}{1-\dfrac{i\Gamma_\nu}{\omega+i\Gamma_\nu}\left[1-\dfrac{\tilde{\chi}^{\nu\nu}(q,\omega+i\Gamma_\nu)}{\tilde{\chi}^{\nu\nu}(\mathbf{q},0)}\right]},\quad \Gamma_\nu=\Gamma_{\nu\nu}, \tag{29}$$

and the interband contributions

$$\chi^{\nu\nu'}=\frac{\tilde{\chi}^{\nu\nu'}(\mathbf{q},\omega+i\Gamma_{12})}{1-(i\Gamma_{12})/(\omega+i\Gamma_{12})[1-[\tilde{\chi}^{12}(\mathbf{q},\omega+i\Gamma_{12})+\tilde{\chi}^{21}(\mathbf{q},\omega+i\Gamma_{12})]/[\tilde{\chi}^{12}(\mathbf{q},0)+\tilde{\chi}^{21}(\mathbf{q},0)]]},\quad \nu\neq\nu',\quad \Gamma_{12}=\Gamma_{21}, \tag{30}$$

where

$$\tilde{\chi}^{\nu\nu'}(\mathbf{q},\omega+i\Gamma_{\nu\nu'})=\frac{e^2}{4\pi^3\varepsilon_0 q^2}\int\frac{d^3k[f_{\nu'}(\mathbf{k}+\mathbf{q}/2)-f_\nu(\mathbf{k}-\mathbf{q}/2)]}{\hbar\omega+i\hbar\Gamma_{\nu\nu'}-[\varepsilon_{\nu'}(\mathbf{k}+\mathbf{q}/2)-\varepsilon_\nu(\mathbf{k}-\mathbf{q}/2)]}G_{\nu\nu'} \tag{31}$$

and

$$G_{\nu\nu'}=|\langle\mathbf{k}-\mathbf{q}/2,\nu|e^{-iqr}|\mathbf{k}+\mathbf{q}/2,\nu'\rangle|^2.$$

f_ν is the Fermi distribution function. The matrix elements $G_{\nu\nu'}(\mathbf{q})$ are given to a good approximation[29] by

$$G_{11}=G_{22}=\tfrac{1}{4}(1+3\cos^2\Theta), \tag{32}$$

$$G_{12}=G_{21}=\tfrac{3}{4}\sin^2\Theta, \tag{33}$$

where Θ is the angle between the vectors $\mathbf{k}-\mathbf{q}/2$ and $\mathbf{k}+\mathbf{q}/2$. Using these expressions, two integrations in the threefold integrals of Eq. (31) can be performed (see Appendix B). For small wave vectors $\mathbf{q}$ the interband contribution Eq. (31) reduces to

$$\tilde{\chi}^{\nu\nu'}(0,\omega+i\Gamma_{\nu\nu'})=\frac{e^2}{2\pi^2\varepsilon_0}\int_0^\infty dk\frac{f_\nu(k)-f_{\nu'}(k)}{\hbar\omega+i\Gamma_{\nu\nu'}-[\epsilon_{\nu'}(k)-\epsilon_\nu(k)]}. \tag{34}$$

In semiconductors that are opaque to the light, the wave vectors $\mathbf{q}_l$ and $\mathbf{q}_s$ are complex. Therefore, the scattering wave vector is not conserved in the scattering process. Wave vectors in the range $\Delta\mathbf{q}=\mathrm{Im}(\mathbf{q}_l)+\mathrm{Im}(\mathbf{q}_s)$ about $\mathrm{Re}(\mathbf{q}_l-\mathbf{q}_s)$ are involved in the scattering process. As shown by several authors,[30–32] the cross section of light scattering in the case of opaque semiconductors and backscattering can be weighted by a Lorentzian function,

$$\overline{I}(q,\omega)=2\pi\alpha\int_0^\infty\frac{I(q',\omega)dq'}{(q-q')+4\alpha^2}. \tag{35}$$

Here, q is the real part of the scattering wave vector ($q=4\pi n/\lambda_L$) inside the scattering volume, and α is the absorption coefficient with $\alpha_L\approx\alpha_S$. The effective depth of crystal that contributes to the light scattering is $1/\alpha$. For $\alpha\to 0$,

$$\overline{I}(q,\omega)=I(q',\omega)\,\delta(q-q') \tag{36}$$

is reobtained.

IV. HOLE CONCENTRATION AND MOBILITY

In the standard method of electrical characterization the Hall coefficient R and the conductivity σ of the samples are measured and the Hall values $p_H=1/eR$ and $\mu_H=R\sigma$ are obtained. Assuming a Hall factor $r=1$ and a one-band model, the values p_H and μ_H agree with the free-hole concentration p and the conductivity mobility μ. However, because these premises are not fulfilled as well in p-type GaAs as in other p-type group-IV and group III-V compounds, considerable deviations between the Hall values and the corresponding conductivity values p and μ are possible. They are characterized in the parabolic valence-band model of heavy and light holes by an effective Hall factor[27]

$$r_{\mathrm{eff}}=p/p_H=\mu_H/\mu=\frac{(1+a^{3/2})(r_1a^{3/2}\beta^2+r_2)}{(1+a^{3/2}\beta)^2}, \tag{37}$$

where the abbreviation $a=m_1/m_2=(p_1/p_2)^{3/2}$ is used. $1/\beta=\mu_2/\mu_1$ describes the mobility enhancement of the light-hole mobility in comparison with that of the heavy ones, the ratio depends on the scattering mechanisms involved and on the temperature. In the case of different scattering mechanisms, Matthiessen's rule can be applied to obtain an estimate of β. r_1 and r_2 are the Hall factors of the single bands.

Unlike the situation for electrons, the Hall factors of holes are difficult to measure, and even more difficult to calculate. Values between 1 and 2.7 of the effective Hall factor in p-type GaAs were deduced from experimental and theoretical work.[33–37] If we use $r_1=r_2=1$ and $\mu_{2p}=\alpha^{3/2}\mu_{1p}$ (Ref. 38) for polar-optic-mode scattering, $\mu_{2\mathrm{D}}=\alpha\mu_{1\mathrm{D}}$ (Ref. 39) for deformation-potential scattering, and $\mu_{2I}=\alpha^{1/2}\mu_{1I}$ (Ref. 38) for ionized impurity scattering, effective Hall factors 5.14, 2.02, and 1.11 would be obtained, respectively, in the case of only one dominant scattering mechanism. These val-

ues reflect the pure ''two-band'' contribution to the effective Hall factor. The damping constants of the light and heavy holes corresponding to these three scattering processes are related by $\Gamma_{2p}=\alpha^{-1/2}\Gamma_{1p}$, $\Gamma_{2D}=\Gamma_{1D}$ and $\Gamma_{2I}=\alpha^{1/2}\Gamma_{1I}$. The relative importance of the different scattering mechanisms for our highly doped samples will be discussed in Sec. VI.

V. EXPERIMENT

The Hall and the Raman measurement taking were performed on small samples (size $3\times5\times0.5$ mm^3) of differently doped GaAs:Zn single crystals. The Hall measurements were carried out in Van der Pauw geometry in a magnetic field of 0.23 T.

The choice of the optimal excitation wavelength of the Raman spectra of the CPPM depends on the carrier concentration. Excitation in the near-infrared region with the laser line at 1.064 μm ensures small absorption and a small wave-vector transfer, which renders the comparison with theoretical cross sections much easier for low carrier concentrations than for excitation with visible light. For the interband part of the dielectric function the expression in Eq. (34) can be used. Moreover, due to the large light penetration depth the contribution of a depletion layer to the Raman signal can be neglected. However, for $p\gtrsim10^{18}$ cm^{-3} and near-infrared excitation, the CPPM are superimposed with strong single-particle scattering, which prevents the analysis of the CPPM.

The intraband and interband contributions of the single-particle scattering contribute to a different extent depending on the hole concentration and the wavelength of the exciting laser. For $p\gtrsim10^{18}$ cm^{-3} the interband scattering between the bands of the light and heavy holes is very significant in the frequency range of the CPPM for excitations with small wave vectors. In this case vertical transitions between the two bands dominate, which are selected by wave-vector conservation. For larger wave vectors diagonal transitions are possible; the interband scattering extends to a broader frequency range and is weaker in the CPPM region. The ranges of dominating intraband and interband transitions depending on hole concentration, wave vector, and temperature are discussed in more detail in Ref. 46. Excitation with laser energies near the direct energy gap of GaAs should be avoided for the Raman measurements of the CPPM. First, the single-particle scattering is enhanced by resonance and second, Fano-like interferences with the single-particle scattering (Ref. 45) renders the CPPM analysis more difficult. It was shown that the interaction causing the Fano-like interference is due to the forbidden Fröhlich mechanism, which contributes to the Raman scattering only under resonance conditions. We therefore used for the heavy doped samples excitation with $\lambda=514.5$ nm far from resonance and could measure the CPPM without disturbing influence of the single excitation spectrum and Fano interferences.

A. $p\gtrsim10^{18}$ cm^{-3}

The Raman spectra were excited with the 514.5-nm line of an Ar^+ laser. Resonance effects are avoided because the energy of this excitation line lies away from critical points of combined densities of states. The laser power was kept at about 20 mW in order to avoid sample heating. The measurements were performed in backscattering geometry from the (001) plane. For the measurements at low temperature the samples were glued with silver paste to a copper cold finger mounted in a cryostat. The scattered light was analyzed with a triple monochromator T64000 (Jobin Yvon) equipped with holographic gratings 1800 lines/mm and detected by a cooled charge-coupled device. The wave-number scale of the spectrometer was calibrated by comparison with the emission lines of a neon lamp. The spectra at T = 300 K were recorded in the additive mode of the spectrometer with a spectral resolution of 1.2 cm^{-1}, the spectra at low temperatures in the subtractive mode with a spectral resolution of 3 cm^{-1}.

B. $p\lesssim10^{18}$ cm^{-3}

The GaAs samples were excited with the 1.064-μm line of a Nd:YAG laser. The scattered light was analyzed with a double monochromator GDM1000 (Carl Zeiss Jena) with 1350 lines/mm gratings and detected with a cooled S1-characteristic-photomultiplier R 632 (Hamamatsu). The spectral resolution was about 1 cm^{-1}.

VI. RESULTS AND DISCUSSION

A. $p\gtrsim10^{18}$ cm^{-3}

From temperature-dependent Hall-effect measurements of the heavily Zn-doped GaAs samples it is concluded that ionized-impurity scattering is by far the most important scattering mechanism. Based on the two-band model of the electrical conductivity from the measured Hall values p_H and μ_H, the carrier concentration p and mobility μ, and the concentration p_1 (p_2) of the heavy (light) holes, their mobilities μ_1 (μ_2) and corresponding damping values Γ_1 (Γ_2) were calculated (see Table II). The unknown damping constant Γ_{12} was taken to be the average of Γ_1 and Γ_2. The material parameters used for the calculations are given in Table I.

With these parameters the Raman scattering efficiency of the CPPM was calculated without any additional free fit parameter. The Raman spectra at $T=300$ K of eight samples with Hall carrier concentrations in the range $p_H=1.5\times10^{18}$ cm^{-3}–9.0×10^{19} cm^{-3} are shown in Fig. 3. For comparison the Raman spectrum of semi-insulating GaAs is enclosed.

The penetration depth of the laser light with the wavelength of 514.5 nm is about 100 nm. Therefore, the Raman spectra of the CPPM are overlaid by the Raman spectra of the LO phonons from the depletion layer. A small contribution (less than 2% of the area of the CPPM in all cases) of the TO phonon can be seen. For backscattering from the (100) plane, the TO phonon is forbidden by the selection rules in a crystal of T_d symmetry. The small TO-phonon contributions could be due to misorientation of the samples. The measured Raman spectra were fitted to the sum of the calculated CPPM, to a LO-phonon contribution from the depletion layer, and to a TO-phonon contribution. The dashed line is the theoretical result for the CPPM according to Eq. (21) with χ_0 from Eq. (26) and χ_i from Eqs. (28)–(30), and (B1)–(B9). The spectra were measured with the laser-beam polarization $\mathbf{e}^l\parallel[110]$ and the scattered-light polarization $\mathbf{e}^s\parallel[110]$.

TABLE II. Characterization of the Zn-doped p-type GaAs samples. p_H and μ_H are the Hall values of the hole concentration and mobility, respectively, determined by Hall measurements at room temperature. p and μ are hole concentration and mobility derived from the Hall values assuming dominating ionized impurity scattering (samples 5 – 12) and combined ionized impurity/phonon scattering (samples 1 – 4) of the carriers. Γ_1 (Γ_2) are the damping constants of the heavy (light) hole plasmons; Γ is the effective plasmon damping. These values were derived from μ.

Sample	p_H (cm^{-3})	μ_H (cm^2/V s)	p (cm^{-3})	μ (cm^2/V s)	Γ (cm^{-1})	Γ_1 (cm^{-1})	Γ_2 (cm^{-1})
1	1.4×10^{17}	246	2.1×10^{17}	164	135	125	182
2	4.8×10^{17}	179	7.2×10^{17}	118	186	173	250
3	8.2×10^{17}	177	1.2×10^{18}	117	188	174	253
4	1.0×10^{18}	160	1.5×10^{18}	107	205	190	276
5	1.5×10^{18}	148	1.7×10^{18}	133	167	152	402
6	2.7×10^{18}	119	3.0×10^{18}	107	203	183	484
7	4.7×10^{18}	105	5.2×10^{18}	94	227	203	538
8	7.2×10^{18}	92	8.0×10^{18}	83	252	222	588
9	1.1×10^{19}	88	1.2×10^{19}	79	266	236	626
10	1.4×10^{19}	75	1.6×10^{19}	67	308	271	717
11	4.5×10^{19}	55	5.0×10^{19}	50	411	353	935
12	9.0×10^{19}	50	1.0×10^{20}	45	450	383	1014

Raman spectra measured at other surfaces and with different polarizations gave evidence that the selection rules are maintained and the momentum of the incident phonons is conserved for Raman scattering. This applies even for the heavily doped samples as shown in Fig. 4 for the case of a sample with $p_H=1.4\times10^{19}$ cm^{-3}. For backscattering from the (001) surface and polarizations of the incident and scattered light parallel to direction [110], the Raman scattering of the CPPM and LO phonons is allowed in accordance with the selection rules [see Fig. 4(a)], and forbidden at crossed polarizations [see Fig. 4(b)].

Whereas in backscattering off the (001) surface with polarizations along the [110] axes the contributions S_A and S_B of the CPPM are allowed, with polarizations parallel to [100] and [010] only S_A contributes. We measured in both configurations, but no remarkable differences in the spectra were observed. Therefore, we conclude that the S_A contribution dominates. This assumption is confirmed by the observation that, in backscattering off the (110) surfaces, independent of the doping level, no band was observed in the parallel/parallel [$\bar{1}10$] polarization, where only the S_B contribution is allowed [see Fig. 4(d) and Eqs. (25) and (26)]. In backscattering off the (110) surface and crossed polarizations parallel to [001] and [$\bar{1}10$] the CPPM and the LO phonon are forbidden, while the TO phonon is allowed. The band observed [see Fig. 4(c)] appears at the position of the TO phonon with 3.1-cm^{-1} bandwidth. The value of 2.6 cm^{-1} obtained after deconvolution with the slit function is not very different from the bandwidth of 2.2 cm^{-1} observed in undoped GaAs.[40] Dominating S_A contributions were observed in CdS,[48] GaP,[49,4] CdTe,[51] ZnO,[52] SiC,[18] as well. For n-type GaAs the two contributions are comparable in intensity.[50] Calculations based on Eqs. (25) and (26) for n-type GaAs and p-type GaAs with the same carrier concentration and characteristic mobilities show that the S_B contribution in p-type GaAs is much smaller mainly due to the larger carrier masses and smaller mobilities. At low carrier concentrations the frequency of the CPPM is slightly enhanced in comparison with the LO-phonon frequency, crossing the gap between the LO and TO phonons with increasing carrier concentration and reaching the TO-phonon frequency at very large ones. The measured frequencies and dampings of the CPPM correspond well to the calculated ones (see Fig. 5).

From the fit of the measured spectra with the sum of the calculated CPPM and LO phonons the depth d of the depletion layer can be estimated. Using the Schottky model we assume that at distance d away from the surface the carrier concentration abruptly rises to the bulk value. Then the depletion layer depth is obtained by

$$d=(1/2\alpha)\ln(1+\kappa) \tag{38}$$

with $\kappa=\kappa_A/\kappa_S$. $\kappa_A=A_L/A_P$ is the ratio of the measured areas of the LO-phonon band from the depletion layer and the CPPM band in the Raman spectrum, $\kappa_S=I_L/I_P$ is the areas ratio of the calculated Raman cross sections from pure LO phonons, and CPPM in a volume element. The depletion layer depths d calculated with Eq. (38) are shown in Fig. 6. Our values are lower than those calculated with the barrier height $e\phi_B=0.5$ eV reported in Ref. 34 according to

$$d=\left(\frac{2\varepsilon_0\varepsilon_S\phi_B}{e^2p}\right)^{1/2}. \tag{39}$$

The accuracy of our fit increases with increasing carrier concentration, indicating that at least at high carrier concentrations the depletion layer is narrower than that predicted by the Schottky model with $e\phi_B=0.5$ eV.

With decreasing temperatures the CPPM are broadened. This is shown for three carrier concentrations in Fig. 7, where the room-temperature Raman spectra are compared with those measured at 10 K. The Raman cross section was calculated with input parameters p and μ derived from Hall measurements of p_H and μ_H using an effective Hall factor

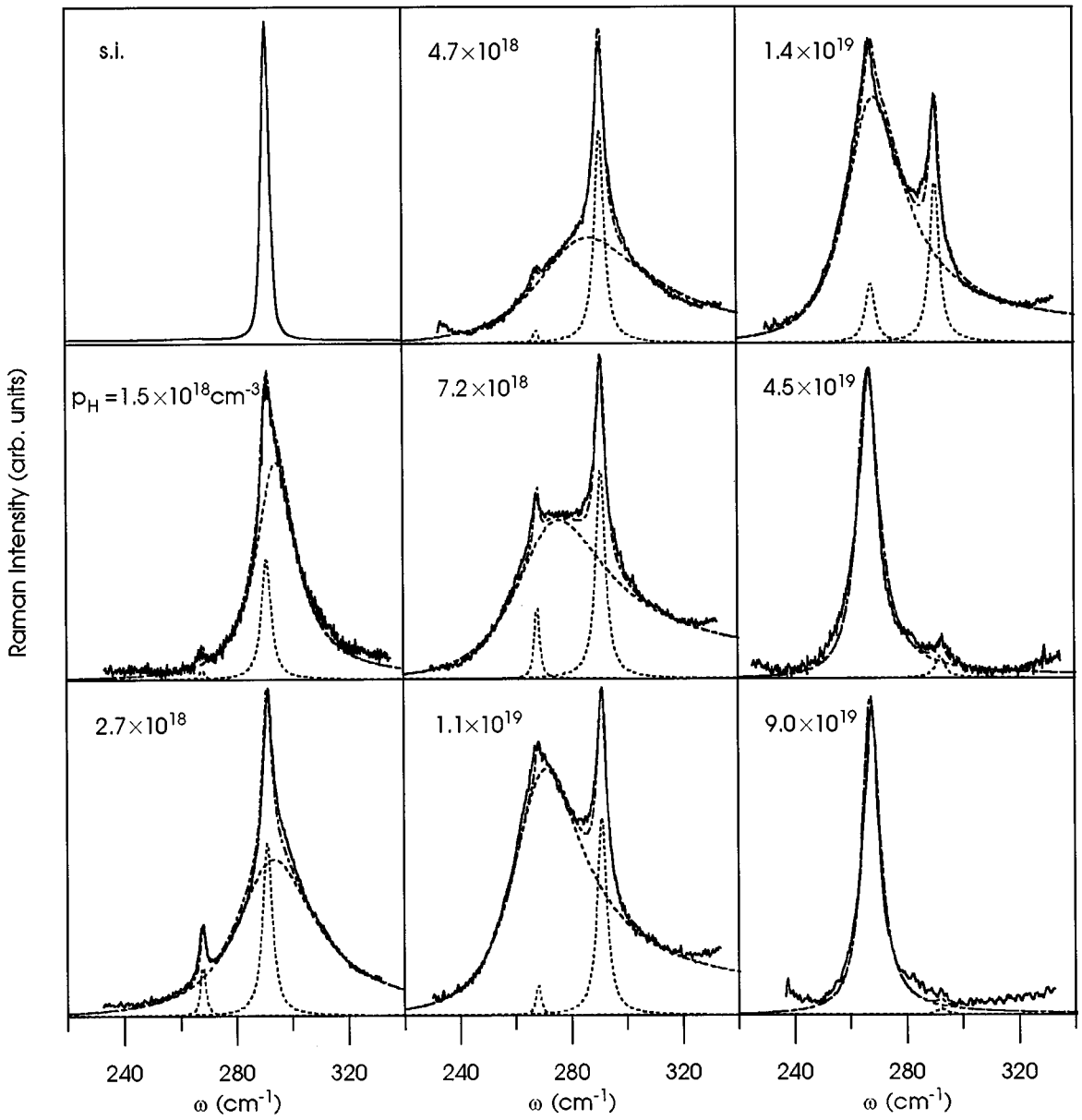

FIG. 3. Raman spectra of the samples characterized in Table II. The Raman spectrum of a semi-insulating sample is included for comparison. The spectra were obtained at room temperature in backscattering. The solid line gives the experimental result, the dashed line the theoretical result for the CPPM according to Eq. (21) with χ_0 from Eq. (26) and χ_i from Eqs. (28)–(30), (B1)–(B9) without additional fit parameters; the dash-dotted line takes into consideration the contribution of the LO phonon (dotted line) from the depletion layer and a small TO-phonon contribution (dotted line).

$r_{\text{eff}}=1.1$ valid for dominating ionized impurity scattering. At low temperatures the contribution of the interband transitions to the dielectric function cannot be neglected.[20] It results in a mode broadening, especially in the concentration range $p_H \lesssim 10^{19}$ cm^{-3}. For comparison, theoretical curves calculated without interband term are given as well.

B. $p \lesssim 10^{18}$ cm^{-3}

Hall measurements of these samples proved the freezing of the free carriers at low temperatures and indicated contributions of phonon scattering to the mobility of the free holes. Therefore, fits of the Raman spectra based on an effective Hall factor $r_{\text{eff}}>1.1$ gave better results than with $r_{\text{eff}}=1.1$, assuming ionized impurity scattering only. Figure 8(a) shows the Raman spectrum of sample 3 excited with 514.5-nm laser light and theoretical Raman cross sections based on $r_{\text{eff}}=1.5$. However, due to the larger depletion layer depth at low carrier concentration and the small frequency shift of the CPPM in comparison with the pure LO-phonon frequency it is difficult to separate the contributions of the bulk CPPM from the depletion layer LO phonon in the measured Raman spectrum. For p-type GaAs with low carrier concentration we therefore excited the Raman spectra with the laser line at 1.064 nm in the transparency region of the samples, where the depletion layer influence can be neglected[26] [see Fig. 8(b)]. In this case, for the theoretical curve Eq. (21) was used with the approximations for small wave vectors in the dielectric function.

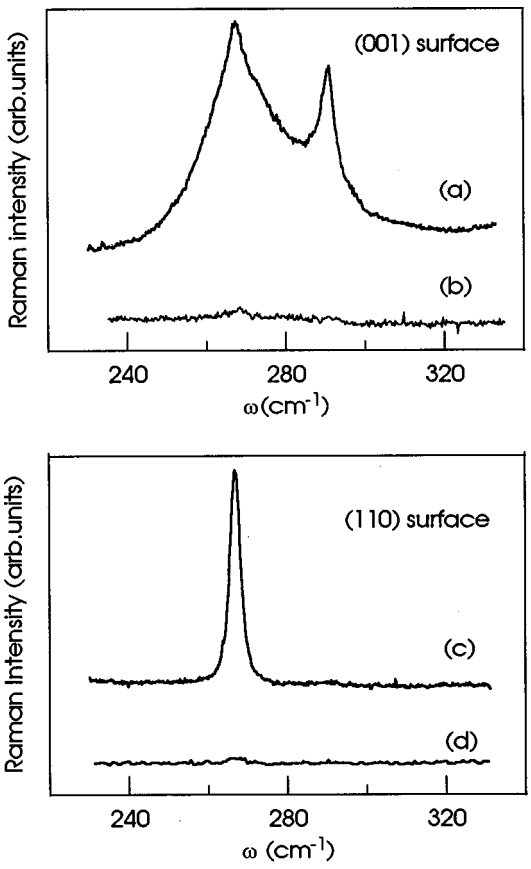

FIG. 4. Raman spectra of the sample with $p_H = 1.4 \times 10^{19}$ cm^{-3} at 300 K measured in backscattering from two surfaces. (a) (001) surface, incident and scattered light polarization ∥ [110]. The spectrum shows the CPPM and the LO phonon from the depletion layer, the TO phonon is forbidden due to the selection rules. (b) (001) surface, incident light polarization ∥ [110], scattered light polarization ∥ [110]. The CPPM, LO phonon, and TO phonon are forbidden. (c) (110) surface, incident light polarization ∥ [001], scattered light polarization ∥ $[\bar{1}10]$. The spectrum shows the TO phonon; the CPPM and the LO phonon are forbidden. (d) (110) surface, incident, and scattered light polarization ∥ [001]. LO and TO phonon are forbidden, the contribution S_B (Eq. 22) of the CPPM is allowed.

Figure 9 presents the temperature dependence of the frequency and the bandwidth of the CPPM of three p-type GaAs samples in comparison with the LO-phonon mode of a semi-insulating sample. The parameters of the measured samples are shown in Table II. We observed no significant changes of the Raman shift and of the halfwidth of the coupled phonon-plasmon mode with decreasing temperature in comparison to the values of the LO-phonon mode of the semi-insulating sample. Hall measurements, however, showed distinct temperature dependences of the hole concentration and of the mobility. Based on these values, the simple Drude theory would predict a narrowing and downshifting of the CPPM with decreasing temperature, as shown for one sample in Fig. 10. The calculations taking into account the interband part of the dielectric function describe the observed temperature dependence well. The spectra show a broadening of the bandwidth with decreasing temperature. That means the decrease of the carrier concentration in the

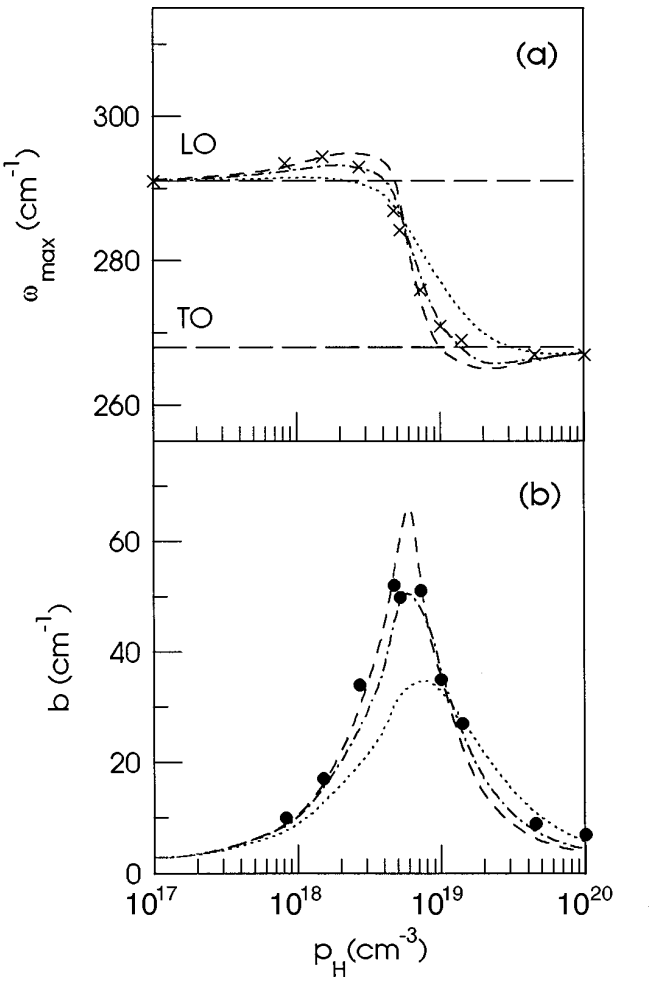

FIG. 5. Energy shift (crosses) and full widths at half height (circles) of the measured CPPM depending on the hole concentration. Theoretical results are drawn for the mobilities $\mu_H = 50$ cm^2/Vs (dotted lines), $\mu_H = 100$ cm^2/Vs (dash-dotted lines), and $\mu_H = 150$ cm^2/Vs (dashed lines).

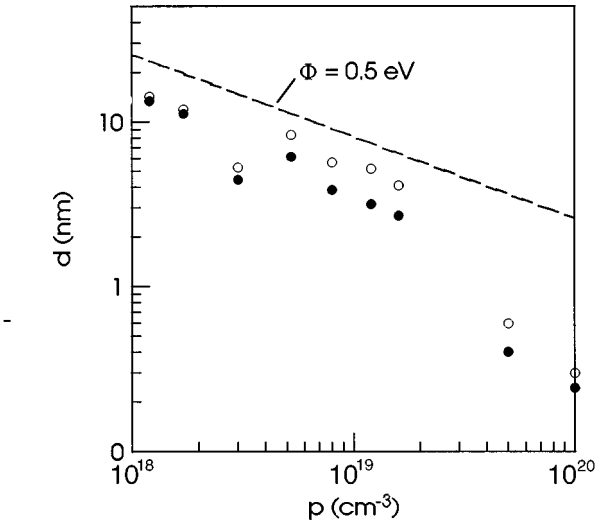

FIG. 6. Depletion layer depth d vs hole concentration p. The calculations using Eq. (38) were performed with $\kappa = \kappa_A / \kappa_S$ (full circles) and $\kappa = \kappa_A$ (open circles). The dashed line was calculated with Eq. (39).

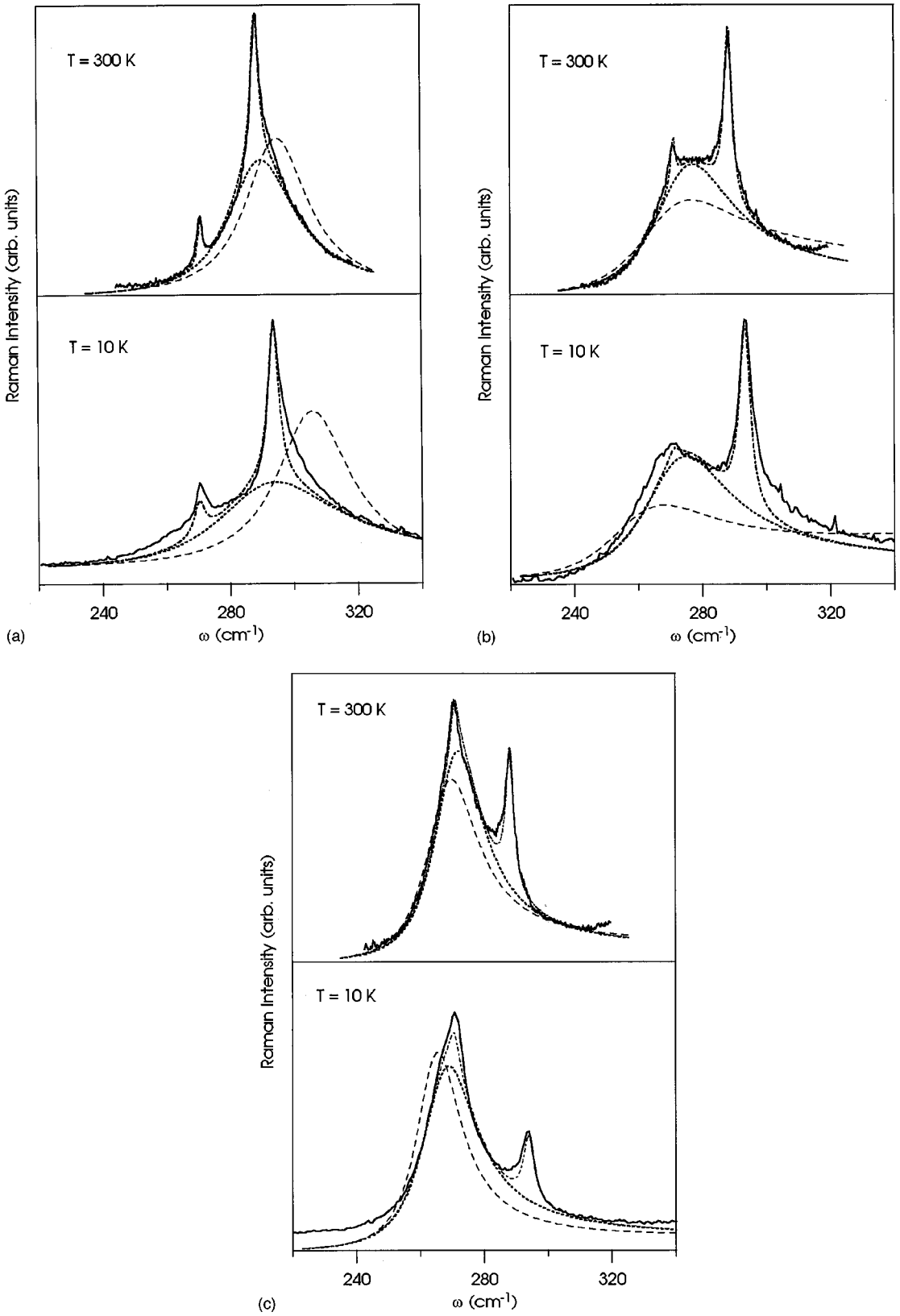

FIG. 7. Raman spectra (solid lines) at two temperatures of the samples with (a) $p_H = 2.7 \times 10^{18}$ cm^{-3} (300 K), (b) $p_H = 7.2 \times 10^{18}$ cm^{-3} (300 K), (c) $p_H = 1.4 \times 10^{19}$ cm^{-3} (300 K) . The theoretical Raman efficiencies of the CPPM are shown by dotted lines. The dash-dotted curves include the contribution of the LO phonon from the depletion layer and a small TO-phonon contribution as well. For comparison the theoretical Raman efficiency of the CPPM without interband contribution (dashed lines) is shown.

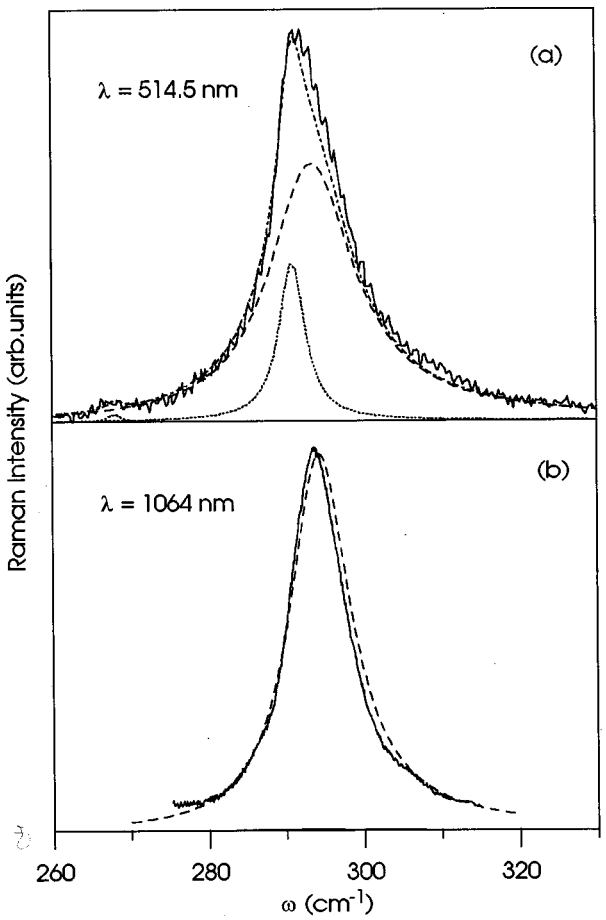

FIG. 8. (a) Raman spectrum (solid line) of sample 3 (characterized in Table II as excited with 514.5 nm. The Raman spectrum was fitted (dash-dotted lines) by the sum of the CPPM contributions (dashed lines) and a LO-phonon contribution from the depletion layer (dotted lines). (b) shows the Raman spectrum excited with 1.064 μm (solid line) and the theoretical Raman efficiency (dash-dotted line).

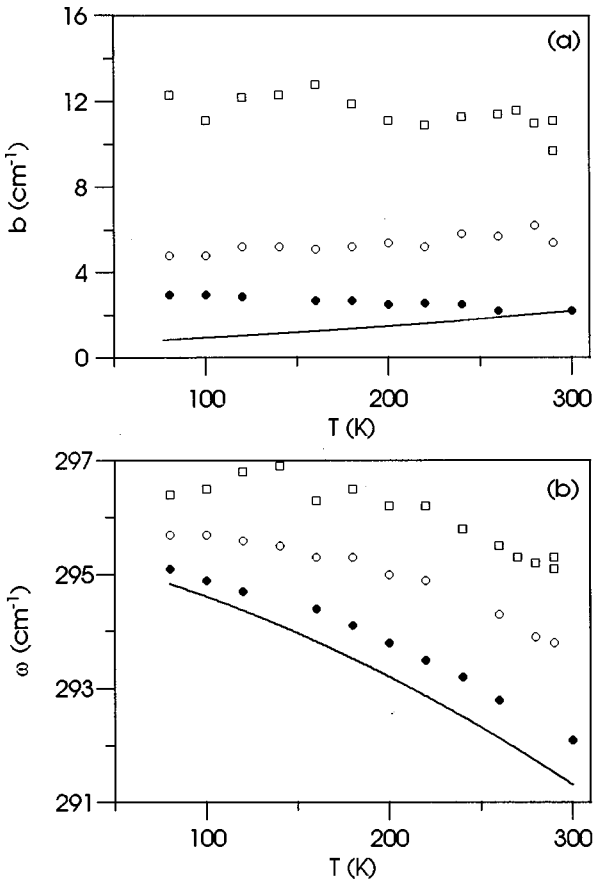

FIG. 9. Raman shift (a) and bandwidth (b) of p-type GaAs samples and of the LO phonon of a semi-insulating sample (solid line) depending on temperature; (●) sample 1, (○) sample 2, (□) sample 4, (●) $p_H = 1.4\times10^{17}$ cm^{-3} (300 K), (○) 4.8×10^{17} cm^{-3} (300 K), (□) 1.0×10^{18} cm^{-3} (300 K).

valence band is compensated by the increasing influence of the interband contribution, which broadens the mode.

The interband part of the dielectric function is enhanced with increased ratio of the effective hole masses $\rho = m_1/m_2$. Therefore, the measurements performed on the p-type GaAs samples with $\rho \approx 7$ were compared with Zn-doped p-type GaP samples with a ratio of about $\rho \approx 3$. In order to realize small absorption, the GaP samples were excited with a Krypton-ion laser at the wavelength 647 nm.

Figure 11 presents the dependence on temperature of frequency and bandwidth of the CPPM in the p-type GaP samples in comparison with the LO-phonon mode of a semi-insulating sample. Both the Raman shift and the bandwidth of the CPPM decrease with decreasing temperature to the values of the LO-phonon mode of the semiinsulating sample. Below 100 K the carrier concentration in the valence band is smaller than 10^{17} cm^{-3} (sensitivity limit of the Raman method).

In this case, the influence of the interband transitions is much smaller, which can be seen by comparison with theoretical curves based on calculations without and with the interband part, respectively. For the sample with $p_H = 8.3\times10^{17}$ cm^{-3} this is shown in Fig. 12.

VII. CONCLUSIONS

The Raman spectra of CPPM in GaAs:Zn were compared with theoretical Raman cross sections in a large doping range. Good agreement was obtained with a theory that takes into account the contributions of heavy and light holes as well as of interband transitions. The interband transitions make an important contribution at low temperatures that results in a broadening of the CPPM. The Raman-scattering efficiencies derived can be used to analyze the CPPM in other polar semiconductors with similar valence-band structures, too. Comparative Raman measurements in p-type GaP:Zn showed a smaller effect that is traced back to the smaller effective-mass ratio of the heavy and light holes. For InP with a mass ratio near that of GaAs ($m_1/m_2 = 4.8$) we expect, e.g., a similar strong influence of the interband contribution to the dielectric function.

ACKNOWLEDGMENTS

The authors would like to thank Professor W. Siegel for helpful discussions. They are indebted to the Freiberger Compound Materials GmbH and to Dr. E. Nowak for supplying samples. Part of this work was supported financially by the Deutsche Forschungsgemeinschaft (Ir 23/1-3).

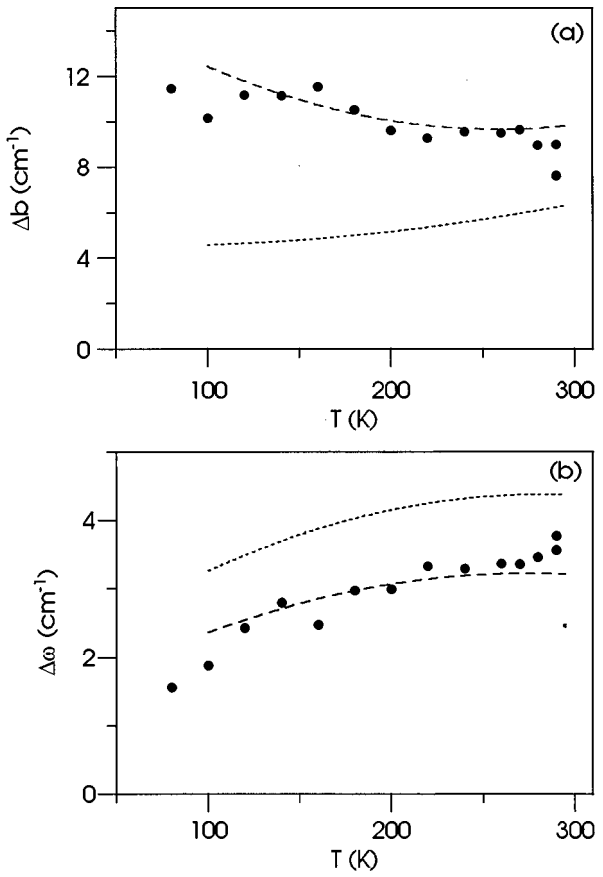

FIG. 10. Relative Raman shift (a) and bandwidth (b) of the p-type GaAs sample 4, with $p_H = 1.0\times10^{18}$ cm^{-3} (300 K) depending on temperature. Raman measurement (●), theoretical results with (dashed line) and without (dotted line) interband contribution included.

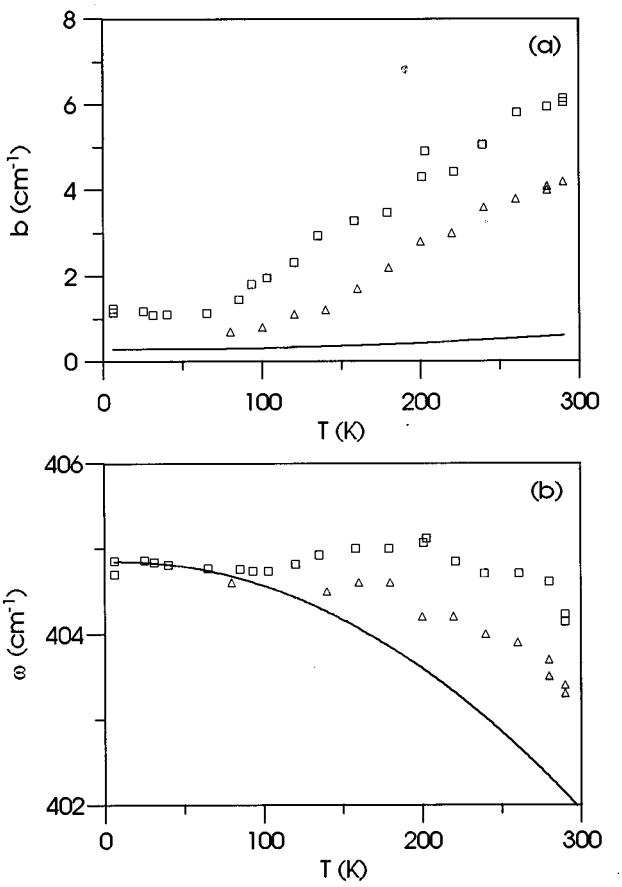

FIG. 11. Raman shift (a) and bandwidth (b) of p-type GaP samples and of the LO phonon of a semi-insulating sample (solid line) depending on temperature, (△) $p_H = 6.5\times10^{17}$ cm^{-3} (300 K), (□) 8.3×10^{17} cm^{-3} (300 K).

APPENDIX A: LIGHT-SCATTERING EFFICIENCY FOR ONE CARRIER TYPE, PHONON DAMPING INCLUDED, $q=0$

In the case of one carrier type with low mobility when only one overdamped CPPM is observed near the LO phonon, and the LO-phonon damping cannot be neglected, the light-scattering efficiency derived from Eqs. (20)–(22) can be written with $\mathrm{Im}(S_A)$ and $\mathrm{Im}(S_B)$ from Eq. (24) and Eq. (25), respectively, but one prefactor in each case has to be changed according to[4]

$$\left[\frac{\omega_T^2(1+C_{\mathrm{FH}}-\omega^2}{\omega_T^2-\omega^2}\right]^2 \Rightarrow 1+2C_{\mathrm{FH}}\omega_T^2[\omega_P^2\Gamma(\omega_T^2-\omega^2) - \omega^2\gamma(\omega^2+\Gamma^2-\omega_P^2)]/N + C_{\mathrm{FH}}^2\frac{\omega_T^4}{\omega_L^2-\omega_T^2}\omega_P^2\{[\Gamma(\omega_L^2-\omega_T^2) + \gamma(\omega_P^2-2\omega^2)] + \omega^2\gamma(\omega+\Gamma^2)\}/N, \tag{A1}$$

and

$$\left(\frac{\omega_L^2-\omega^2}{\omega_T^2-\omega^2}\right)^2 \Rightarrow [\omega_P^2\Gamma(\omega_L^2-\omega^2)^2+\omega_P^2\Gamma(\omega_L^2-\omega_T^2) + \Gamma\gamma^2\omega_P^2\omega^2]/N \tag{A2}$$

with

$$N=\omega_P^2\Gamma[(\omega_T^2-\omega^2)^2+\omega^2\Gamma^2]+\omega^2\gamma(\omega_L^2-\omega_T^2)(\omega^2+\Gamma^2). \tag{A3}$$

APPENDIX B: INTRABAND AND INTERBAND CONTRIBUTIONS TO THE DIELECTRIC FUNCTION

In this appendix we analyze Eq. (31). Using the matrix elements $G_{\nu\nu'}$ given in Eqs. (32) and (33), two integrations in Eq. (31) can be performed, and we arrive at the following expressions for the intraband part:

$$\tilde{\chi}^{\nu\nu}=c_1 y^{-3/2}\int_{x=0}^{\infty} f(x)dx\left\{\ln\frac{(y+\tilde{\Omega}+2\sqrt{xy})}{(y+\tilde{\Omega}-2\sqrt{xy})} \times\frac{(y-\tilde{\Omega}+2\sqrt{xy})}{(y-\tilde{\Omega}-2\sqrt{xy})}+\frac{3}{2}\sqrt{\frac{y}{x}} - \frac{3}{4}\frac{(x-y)^2}{(x^2-\tilde{\Omega}^2)}\ln\left|\frac{\sqrt{x}+\sqrt{y}}{\sqrt{x}-\sqrt{y}}\right|\right.$$

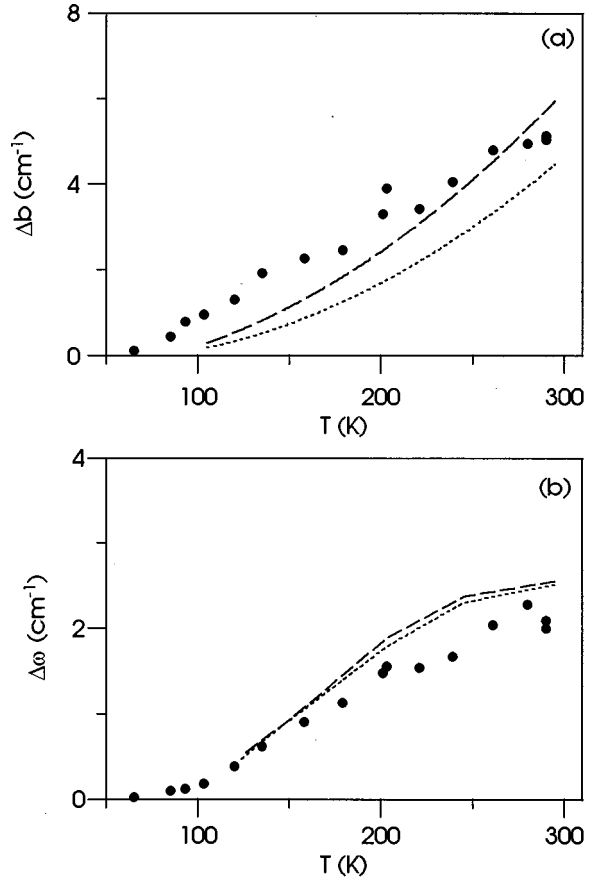

FIG. 12. Relative Raman shift (a) and bandwidth (b) of the p-type GaP sample with $p_H = 8.3\times10^{17}$ cm^{-3} (300 K) depending on temperature. Raman measurement (●), theoretical results with (dashed line) and without (dotted line) interband contribution included.

$$+\frac{3}{16}\frac{[(y+\tilde{\Omega})^2-4xy]}{(x-\tilde{\Omega})}\ln\frac{y+\tilde{\Omega}+2\sqrt{xy}}{y+\tilde{\Omega}-2\sqrt{xy}}$$
$$+\frac{3}{16}\frac{[(y-\tilde{\Omega})^2-4xy]}{(x+\tilde{\Omega})}\ln\frac{y-\tilde{\Omega}+2\sqrt{xy}}{y-\tilde{\Omega}-2\sqrt{xy}}, \tag{B1}$$

and for the interband part,

$$\tilde{\chi}^{\nu'\nu}=\frac{c_1}{y^{3/2}}\int_{x=0}^{\infty}dx\left\{-\frac{3}{4}\sqrt{\frac{y}{x}}[\rho f_\nu(x)+f_{\nu'}(x)]\right.$$
$$+\frac{3(x-y)^2}{8x}\left[\frac{f_\nu(x)}{(x-\tilde{\Omega})}+\frac{f_{\nu'}(x)}{(x/\rho+\tilde{\Omega})}\right]\ln\left|\frac{\sqrt{x}+\sqrt{y}}{\sqrt{x}-\sqrt{y}}\right|$$
$$-\frac{3f_\nu(x)\{[y+\rho\tilde{\Omega}-(\rho-1)x]^2-4xy\}}{16x(x-\tilde{\Omega})}$$
$$\times\ln\frac{y+\rho\tilde{\Omega}-(\rho-1)x+2\sqrt{xy}}{y+\rho\tilde{\Omega}-(\rho-1)x-2\sqrt{xy}}$$
$$-\frac{3f_{\nu'}(x)\{[y-\tilde{\Omega}+(\rho-1)x/\rho]^2-4xy\}}{16x(x/\rho+\tilde{\Omega})}$$
$$\left.\times\ln\frac{y-\tilde{\Omega}+(\rho-1)x/\rho+2\sqrt{xy}}{y-\tilde{\Omega}+(\rho-1)x/\rho-2\sqrt{xy}}\right\}. \tag{B2}$$

The following abbreviations were used:

$$c_1=\frac{e^2\sqrt{m_\nu^*}}{4\pi^2\varepsilon_0\hbar\sqrt{2k_BT}}, \tag{B3}$$

$$x=\frac{\varepsilon}{k_BT}=\frac{\hbar^2k^2}{2m_\nu^*k_BT}, \tag{B4}$$

$$y=\frac{\hbar^2q^2}{2m_\nu^*k_BT}, \tag{B5}$$

$$\tilde{\Omega}=\frac{\hbar\tilde{\omega}}{k_BT}, \tag{B6}$$

$$\tilde{\omega}=\omega+i\Gamma_{\nu\nu'}, \tag{B7}$$

$$\rho=\frac{m_{\nu'}}{m_\nu}, \tag{B8}$$

$$f_\nu(x)=[1+\exp(x+\mu)]^{-1}, \tag{B9}$$

where μ is the chemical potential.

[1] B. B. Varga, Phys. Rev. A **137**, 1896 (1965).
[2] A. Mooradian and G. B. Wright, Phys. Rev. Lett. **16**, 999 (1966).
[3] D. T. Hon and W. L. Faust, Appl. Phys. **1**, 241 (1973).
[4] G. Irmer, V. V. Toporov, B. H. Bairamov, and J. Monecke, Phys. Status Solidi B **119**, 595 (1983).
[5] W. Bala, F. Firszt, M. Grinberg, M. Drozdowski, and M. Kozielski, Acta Phys. Pol. A **75**, 75 (1989).
[6] H. Yugami, S. Nakashima, K. Sokai, H. Kojima, M. Hangyo, and A. Mitsuishi, J. Phys. Soc. Jpn. **56**, 1881 (1987).
[7] S. Nakashima, H. Yugami, A. Fujii, and M. Hangyo, J. Appl. Phys. **64**, 3067 (1988).
[8] D. Olego and M. Cardona, Phys. Rev. B **24**, 7217 (1981).
[9] T. Kamijoh, A. Hashimoto, H. Takano, and M. Sakuta, J. Appl. Phys. **59**, 2382 (1986).
[10] T. Yuasa and M. Ishii, Phys. Rev. B **35**, 3962 (1987).
[11] A. Mlayah, R. Carles, G. Landa, E. Bedel, and A. Muñoz-Yagüe, J. Appl. Phys. **69**, 4064 (1991).
[12] K. Wan and J. F. Young, Phys. Rev. B **41**, 10 772 (1990).
[13] M. V. Klein, in *Light Scattering in Solids I*, edited by M. Cardona (Springer-Verlag, Berlin, 1983), p. 147.
[14] W. Bardyszewski, Solid State Commun. **57**, 873 (1986).
[15] R. Fukasawa and S. Perkowitz, Phys. Rev. B **50**, 14 119 (1994).
[16] M. Gargouri, B. Prevot, and C. Schwab, J. Appl. Phys. **62**, 3902 (1987).
[17] G. Irmer, J. Monecke, W. Siegel, G. Kühnel, B.H. Bairamov, and V. V. Toporov, in *Proceeedings of the 13th International Conference on Raman Spectroscopy*, edited by W. Kiefer, M. Car-

dona, G. Schaack, F. W. Schneider, and H. W. Schrötter (Wiley, Chichester, 1992).
[18] M. V. Klein, B. N. Ganguly, and P. J. Colwell, Phys. Rev. B **6**, 2380 (1972).
[19] N. D. Mermin, Phys. Rev. B **1**, 2362 (1970).
[20] G. Irmer and J. Monecke (unpublished).
[21] S. S. Iha, Nuovo Cimento B **63**, 331 (1969); Comments Solid State Phys. **4**, 111 (1972).
[22] A. Pinczuk and E. Burstein, in *Light Scattering in Solids I* (Ref. 13), p. 23.
[23] G. Abstreiter, M. Cardona, and A. Pinczuk, in *Light Scatttering in Solids IV*, edited by M. Cardona and G. Güntherodt (Springer-Verlag, Berlin, 1984), p. 5.
[24] P. M. Platzman and P. A. Wolff, *Waves and Interactions in Solid Plasmas* (Academic Press, New York, 1973).
[25] M. Born and K. Huang, *Dynamical Theory of Crystal Lattices* (Clarendon Press, Oxford, 1962).
[26] M. Giehler and E. Jahne, Phys. Status Solidi B **73**, 503 (1976).
[27] G. Irmer, W. Siegel, G. Kühnel, J. Monecke, F. M. M. Yasuoka, B. H. Bairamov, and V. V. Toporov, Semicond. Sci. Technol. **6**, 1072 (1991).
[28] J. Monecke, Phys. Status Solidi B **121**, 329 (1984).
[29] M. Combescot and P. Nozières, Solid State Commun. **10**, 301 (1972).
[30] D. L. Mills, A. A. Maradudin, and E. Burstein, Ann. Phys. (N.Y.) **56**, 504 (1970).
[31] R. Zeyher, C. S. Ting, and J. L. Birman, Phys. Rev. B **10**, 1725 (1974).
[32] G. Abstreiter, R. Trommer, M. Cardona, and A. Pinczuk, Solid State Commun. **30**, 703 (1979).
[33] H. J. Lee and D. C. Look, J. Appl. Phys. **54**, 4446 (1983).
[34] L. A. Borisova, A. F. Kravcenko, K. N. Kot, and E. M. Skok, Fiz. Tekh. Poluprovodn. **6**, 799 (1972) [Sov. Phys. Semicond. **6**, 693 (1972)].
[35] H. Neumann and Van Nam Nguyen, Krist. Tech. **13**, 211 (1978).
[36] K. Takeda, N. Matsumoto, A. Taguchi, H. Taki, E. Ohta, and M. Sokata, Phys. Rev. B **B32**, 1101 (1985).
[37] L. Gouskov, S. Bilac, J. Pimentel, and A. Gouskov, Solid-State Electron. **28**, 653 (1977).
[38] K. Somogyi, Phys. Status Solidi A **37**, 653 (1976).
[39] J. D. Wiley and M. D. Domenico, Phys. Rev. B **2**, 427 (1970).
[40] G. Irmer, M. Wenzel, and J. Monecke, Phys. Status Solidi B **195**, 85 (1996).
[41] D. E. Aspnes and A. A. Studna, Phys. Rev. B **27**, 985 (1983).
[42] J. S. Blakemore, Appl. Phys. **53**, R123 (1982).
[43] S. Zekeng, B. Prevot, and C. Schwab, Phys. Status Solidi B **150**, 65 (1988).
[44] M. S. Skolnick, A. K. Jain, R. A. Stradling, J. Leotin, J. C. Ousset, and S. Askenazy, J. Phys. C **9**, 2809 (1976).
[45] G. Irmer, M. Wenzel, and J. Monecke, in *Proceedings of the 23rd International Conference on the Physics of Semiconductors* (World Scientific, Singapore, 1996), p. 217.
[46] G. Irmer, J. Monecke, and M. Wenzel, J. Phys. Condens. Matter **9**, 5371 (1997).
[47] J. Menéndez and M. Cardona, Phys. Rev. B **31**, 3696 (1985).
[48] J. F. Scott, T. C. Damen, J. Ruvalds, and J. Zawadowski, Phys. Rev. B **3**, 1295 (1971).
[49] D. T. Hon and W. L. Faust, Appl. Phys. **1**, 241 (1973).
[50] A. Mooradian and A. L. McWhorter, in *Light Scattering Spectra of Solids*, edited by G. B. Wright (Springer-Verlag, New York, 1968), p. 297.
[51] B. H. Bairamov, G. Irmer, J. Monecke, V. V. Toporov, N. V. Agrinskaja, and S. A. Samedov, Fiz. Tverd. Tela **29**, 2201 (1987) [Sov. Phys. Solid State **29**, 1270 (1987)].
[52] B. H. Bairamov, A. Heinrich, G. Irmer, V. V. Toporov, and E. Ziegler, Phys. Status Solidi B **119**, 227 (1983).
[53] R. F. Wallis and M. Balkansi, *Many-Body Aspects of Solid State Spectroscopy* (North-Holland, Amsterdam, 1986).